D-Band Total Power Radiometer Performance Optimization in an SiGe HBT Technology

E. Dacquay, *Student Member, IEEE*, A. Tomkins, K. H. K. Yau, *Member, IEEE*, E. Laskin, Pascal Chevalier, *Member, IEEE*, A. Chantre, *Senior Member, IEEE*, B. Sautreuil, and S. P. Voinigescu, *Senior Member, IEEE*

***Abstract*—A D-band SiGe HBT total power radiometer is reported with a peak responsivity of 28 MV/W, a noise equivalent power (NEP) of 14–18 fW/Hz$^{1/2}$, and a temperature resolution better than 0.35 K for an integration time of 3.125 ms. The $1/f$ noise corner of the radiometer is lower than 200 Hz. Fabricated in a developmental technology with 270-GHz f_T and 330-GHz $f_{\rm MAX}$, it includes a five-stage low-noise amplifier (LNA) with 4–7-GHz bandwidth and over 35 dB of gain centered at 165 GHz, along with a square-law detector with an NEP below 6 pW/Hz$^{1/2}$ up to 170 GHz. An average system noise temperature of 1645 K is obtained using the Y-factor method and a noise bandwidth of 10 GHz calculated from the measured $S21(f)$ characteristics of the radiometer. The reduced $1/f$ noise corner frequency in the presence of the amplifier, compared to that of the detector, appears to indicate that, unlike in III–V radiometers, LNA gain fluctuations are not a problem in SiGe HBT radiometers. The circuit consumes 95 mW and occupies 765 $\times$ 490 μm^2. Wafer mapping of the radiometer sensitivity and of the amplifier gain was performed across different process splits. The mapping results demonstrate that the radiometer can be employed as a relatively simple and area-efficient transistor noise-measure monitor, useful in SiGe HBT vertical profile optimization.**

***Index Terms*—D-band, detector, low-noise amplifier (LNA), noise equivalent power (NEP), noise equivalent temperature difference (NETD), noise figure, $1/f$ noise corner, passive imaging, radiometer, responsivity, SiGe HBT.**

I. Introduction

THE D-band total power radiometer is attractive for applications such as stand-off security screening [1] and for atmospheric water cycle and hurricane monitoring at 118 and 183 GHz [2]. Since the angular resolution of a lens or aperture improves with decreasing wavelength [3], D-band passive imaging arrays have excellent potential for high-resolution operation without requiring electronic or mechanical switching or local oscillator (LO) signal distribution [4]. Unlike other currently available semiconductor technologies, advanced SiGe BiCMOS with thick-metal, thick dielectric back-end-of-line (BEOL), and $f_{\rm MAX}$ values now approaching 500 GHz [5] allow wafer-scale antenna array integration with over 50% antenna efficiency [6], [7]. While presently there are no reported commercial solid-state passive imagers in the D-band, five commercial W-band systems have recently appeared on the market [8]. These are typically realized using discrete amplifiers with over 35-dB gain and noise figures below 5 dB, followed by a zero-bias diode (ZBD) detector chip, all fabricated in III–V technologies [4], [9].

In total power radiometers, the amplifier gain fluctuations, which manifest themselves as $1/f$ noise, and the $1/f$ noise of the detector, are as critical as the amplifier noise figure in determining the overall temperature sensitivity [4]. Image calibration is performed by pointing to a reference temperature source, thus avoiding mechanical chopping or integration of a switch, which would reduce sensitivity [1].

Recently, W-band total power radiometers have been reported in SiGe HBT [10], [11] and CMOS [12] technologies, demonstrating promising temperature sensitivity and noise performance. A number of III–V heterodyne receivers [13], [14] and even a super-regenerative CMOS receiver [2] have been published or announced, which operate in the D- and G-bands with excellent noise performance. However, they require oscillators or LO signal distribution and will not be considered in this paper.

Cutting-edge SiGe HBT technologies, in particular, with the lowest $1/f$ noise corner of all competing technologies, represent an interesting opportunity where the high-volume benefits of silicon can be exploited while also taking advantage of RF device performance with high gain even in the D- and G-bands [15]–[18]. In this paper, we report the first D-band total power radiometer with high-gain pre-amplification fabricated in silicon. Its $1/f$ noise corner, low-noise amplifier (LNA) gain, detector noise equivalent power (NEP), and overall imager sensitivity are comparable to those of the best III–V total power radiometers and detectors operating at W-band. In an effort to identify the key semiconductor technology figures of merit that impact the total power radiometer sensitivity, we also conduct a comprehensive study across process splits of transistor f_T, $f_{\rm MAX}$, amplifier gain, noise figure, detector responsivity, NEP, and $1/f$ noise corner, separating them from system parameters unrelated to the technology, such as integration time and frame

Manuscript received August 02, 2011; revised December 22, 2011; accepted December 23, 2011. This work was supported by the National Science and Engineering Research Council (NSERC) of Canada.

E. Dacquay and S. P. Voinigescu are with the Edward S. Rogers Sr. Department of Electrical and Computer Engineering, University of Toronto, Toronto, ON, Canada M5S 3G4 (e-mail: dacquaye@eecg.toronto.edu).

A. Tomkins and E. Laskin were with the Edward S. Rogers Sr. Department of Electrical and Computer Engineering, University of Toronto, Toronto, ON, Canada M5S 3G4. They are now with Peraso Technologies Inc., Toronto, ON, Canada M5J 2L7.

K. H. K. Yau was with the Edward S. Rogers Sr. Department of Electrical and Computer Engineering, University of Toronto, Toronto, ON, Canada M5S 3G4. He is now with the Broadcom Corporation, Irvine, CA 92617 USA.

P. Chevalier, A. Chantre, and B. Sautreuil are with STMicroelectronics, F-38926 Crolles, France (e-mail: pascal.chevalier@st.com).

Color versions of one or more of the figures in this paper are available online at http://ieeexplore.ieee.org.

Digital Object Identifier 10.1109/TMTT.2012.2184132

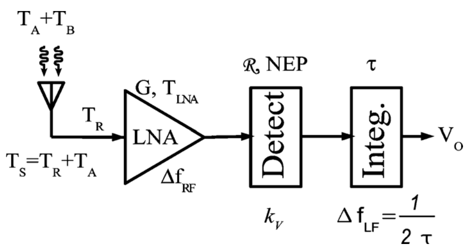

Fig. 1. Block diagram and system performance parameters of an integrated total power radiometer.

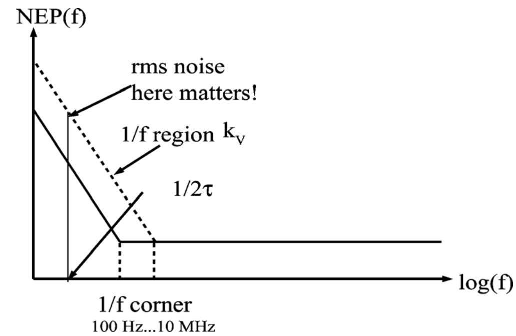

Fig. 2. Typical output noise spectra for semiconductor III–V SBD, SiGe (solid), and CMOS (dashed) detectors [4], [10], [12].

rate. The circuits were fabricated in a preproduction 130-nm SiGe BiCMOS technology (BC9MW) and in two experimental SiGe HBT technologies: B3T and B4T.

This paper is organized as follows. In Section II, we discuss system and circuit design considerations and implementation problems. This is followed by a description of the fabrication process and transistor characterization in Section III. Detailed S-parameter and $1/f$ noise characterization of the amplifier and detector breakouts across process splits is covered in Section IV, along with a hot–cold noise source method to measure the radiometer the noise-equivalent differential temperature (NEDT) and effective system noise temperature in Section V. Conclusions are summarized in Section VI.

II. System and Circuit Design Considerations

A. Total Power Radiometer Design Considerations

Passive imaging sensors or radiometers are high-sensitivity broadband receivers used to measure the thermal ("black-body") radiation (noise) emitted or reflected by a target. A body in thermal equilibrium at a temperature T emits energy according to Planck's radiation law

$$P = k\Delta f T \tag{1}$$

where Δf is the receiver bandwidth over which the black body radiation is integrated and k is the Boltzmann's constant.

This equation is strictly valid only for a perfect "black body" that absorbs all incident energy and reflects none. A nonideal object partially reflects incident energy and radiates only a fraction of the energy predicted by (1). It can therefore be described by a "brightness" (noise) temperature, T_B, which is always smaller than its physical temperature and much smaller than the receiver noise temperature T_R.

This radiation is very weak at millimeter-wave frequencies, and therefore, sensitivity becomes the most important design parameter for a radiometer. Most modern W-band [4], [8] "cameras" employ a direct detection (or tuned homodyne) receiver, also known as a *total power radiometer*, consisting of an LNA, a square-law detector, a post-detector low-bandwidth "video" amplifier, and an integrator, as in Fig. 1. A 2-D image is formed by mechanically steering the antenna in the X- and Y-directions and recording the image at each position. This is a slow process. Ideally, if low-cost and low-power receivers could be developed, mechanical steering would be replaced by a 2-D receiver array to achieve electronic scanning and image collection at a much faster rate.

The system performance of a total power radiometer is determined by the following:

- the antenna and implementation loss, captured by T_A;
- the gain G, bandwidth Δf_{RF}, and noise figure (equivalent noise temperature T_{LNA}) of the LNA;
- the responsivity $\mathcal{R}$, $1/f$ noise slope, k_V, and NEP of the detector (Fig. 2), where $S_{vf} = k_V(V^2/f)$ describes the $1/f$ noise of the detector diode [4];
- the integration time τ (or bandwidth $\Delta f_{LF} = 1/2\tau$) of the integrator.

The system bandwidth Δf is given by the entire receive-chain preceding the detector and is typically determined by the LNA.

The imager resolution in degrees Kelvin can be expressed as [9]

$$\Delta T_{\mathrm{MIN}} = (T_A + T_R)\sqrt{\frac{1}{\Delta f_{\mathrm{RF}}\tau} + \frac{k_V}{G}\ln N + \left(\frac{\Delta G}{G}\right)^2} \tag{2}$$

where $N = T_{\mathrm{frame}}/\tau$ [4] represents the numbers of pixels in a frame, and T_{frame} describes the video frame rate, typically 6–30 Hz [1]–[4], [8]. For an imaging system with a single pixel, $N = 1$ and the second term in (2) disappears. ΔT_{MIN} is also known as the noise equivalent temperature difference (NETD) [9].

Equation (2) indicates that, in order to improve resolution, the system noise temperature must be reduced and the integration time and RF bandwidth must be increased. Fluctuations in noise at frequencies higher than $1/2\tau$(first term under the radical) are smoothed out through the integration process. The $1/f$ noise from the detector diode at frequencies below $1/2\tau$, divided by the LNA gain, and from the amplifier gain fluctuations, if any, are captured by the second and third terms, respectively, under the square root [4], [9]. Indeed, a critical aspect of radiometer design is the development of a detector with very low $1/f$ noise corner and of an amplifier with low noise figure, high gain, and no gain fluctuations. While the first three goals are readily satisfied in III–V radiometers, the fourth remains elusive since considerable $1/f$ noise is still present in the output spectra of even the best-performing systems with low $1/f$ noise detectors, over 30–35-dB LNA gain, and less than 5-dB noise figure [4].

The proposed SiGe HBT total-power radiometer, whose transistor-level schematic is shown in Fig. 3, consists of a single-ended five-stage LNA, similar to the one in [15] and centered at 165 GHz, followed by a differential square-law detector. A

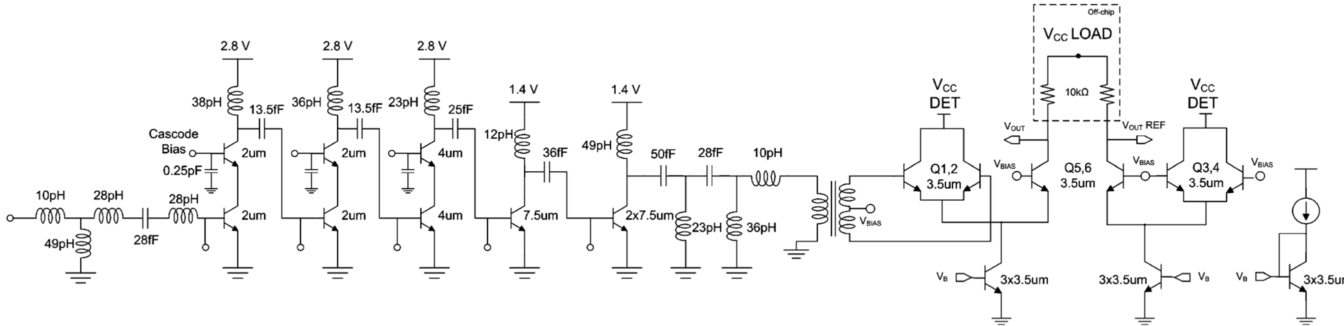

Fig. 3. Transistor-level schematics of integrated total power radiometer.

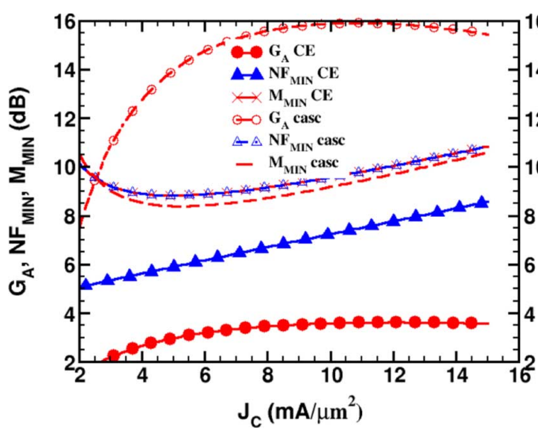

Fig. 4. Simulated $\mathrm{NF}_{\min}$. $M_{\min}$ and available gain for 110 nm × 4.5 μm B4T CE and cascode stages at 165 GHz.

transformer is used for single-ended to differential conversion between the LNA and detector.

B. Amplifier Topology Selection and Design

The LNA poses significant challenges at D-band in any technology because it must simultaneously achieve very high gain (over 30 dB), broad bandwidth, and low noise figure. The high gain is needed to overcome the large $1/f$ noise of the detector at video-rate frequencies: 10–60 Hz.

A simulation study of the available gain, minimum noise figure, and minimum noise measure of common emitter (CE) and cascode stages was conducted and the simulation results at 165 GHz versus collector current density are reproduced in Fig. 4 for the B4T technology. Although the noise figure of the CE stage is significantly smaller, the two topologies have almost identical minimum noise measures of 8.8 and 8.4 dB, respectively, favoring the cascode. Moreover, the corresponding available gain is 14 dB for the cascode and 3 dB for the CE stage. Consequently, at least one or two cascode stages must be employed to achieve the much needed high gain at D-band without excessive power consumption. However, an SiGe HBT cascode is prone to oscillate if its emitter length and bias current are larger than 4–5 μm and 6–8 mA, respectively. In contrast, CE stages exhibit excellent stability.

Recent transistor and receiver noise-figure measurements show promising SiGe HBT values, below 5 dB up to 170 GHz [16], and cascode amplifier noise figures around 8 dB [16], [17]. However, the experimental data indicate that the design kit model overestimates the minimum noise figure. For these reasons, topologies with approximately equal gain and a combination of five CE and cascode stages, placed either at the input or at the output of the amplifier, were fabricated and investigated for the lowest overall noise figure.

The first amplifier, A, employed in the radiometer of Fig. 3, was originally designed as a general-purpose moderate output power amplifier [15] in a production process (BC9MW) [19] and was ported without redesign into two developmental process technologies (B3T [20] and B4T) intermediary development steps as part of the dot5 European Union (EU) program [5]. This amplifier consists of three low-current cascode stages, followed by two large-current CE stages. The simulated noise figure and power gain at 165 GHz for the B4T process are plotted in Fig. 5 as a function of the collector current density in the first cascode stage. As can be seen, the noise figure and gain are 11 and 37 dB, respectively, when the first stage is biased at the optimum noise figure current density of 6 mA/μm^2, This current density is 30% higher than that in Fig. 4, likely because of the loading from the other stages and from the layout parasitics, which were not included in the simulations of the individual stage. The amplifier consumes 140 mW from 1.5- and 3-V supplies in BC9MW, and 92 mW from 1.4- and 2.8-V supplies in B4T. Lumped inductors, designed and modeled using ASITIC,[1] and a mix of custom-designed metal–oxide–metal (MOM) capacitors and foundry-provided metal–insulator–metal (MIM) capacitors, were employed for all tuning and matching elements. The three low bias current cascode stages provide significant gain, and due to the small input stage transistor size, broadband matching to 50 Ω. The two CE stages, with lower gain, are designed to provide higher linearity and large saturated output power with improved stability.

The second LNA, B, shown in Fig. 6, consists of two CE stages followed by three cascode stages. It consumes 75 mW from 1.5- and 3-V supplies. Apart from the degeneration inductor in the first stage, it employs microstrip transmission lines as matching elements. The microstrip lines are realized in the top metal layer with a 1-μm-thick ground plane formed by shunting the first two metal layers together to reduce ground loss, as illustrated in Fig. 7. Emitter degeneration resistors, bypassed at D-band, provide improved bias current accuracy and stability over PVT variations. The simulated gain and noise figure are reproduced in Fig. 8 as a function of the collector current density in the first stage. The minimum noise figure

[1][Online]. Available: http://rfic.eecs.berkeley.edu/~niknejad/asitic.html

This article has been accepted for inclusion in a future issue of this journal. Content is final as presented, with the exception of pagination.

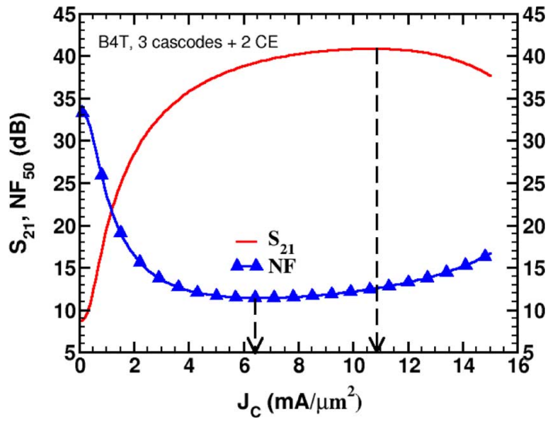

Fig. 5. Simulated NF_{50} and S_{21} at 165 GHz as a function of collector current density for amplifier A in the B4T process.

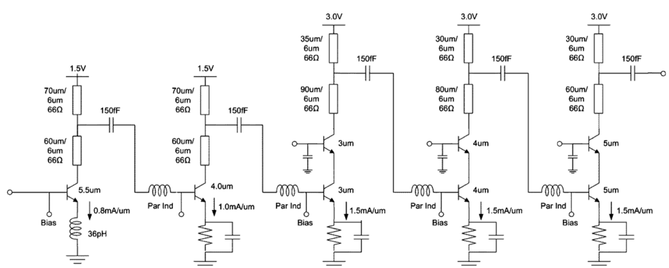

Fig. 6. Schematics of amplifier B with CE input stage and t-lines in BC9MW.

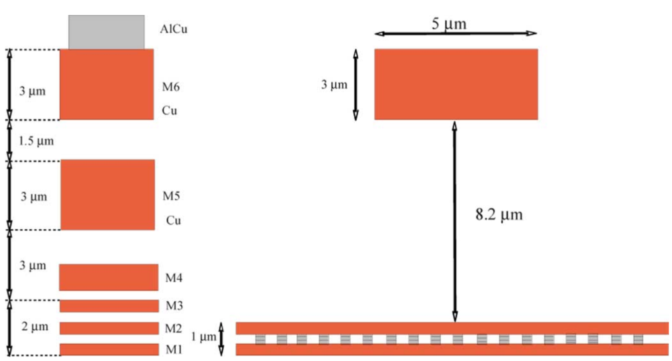

Fig. 7. Microstrip-line and back-end cross sections.

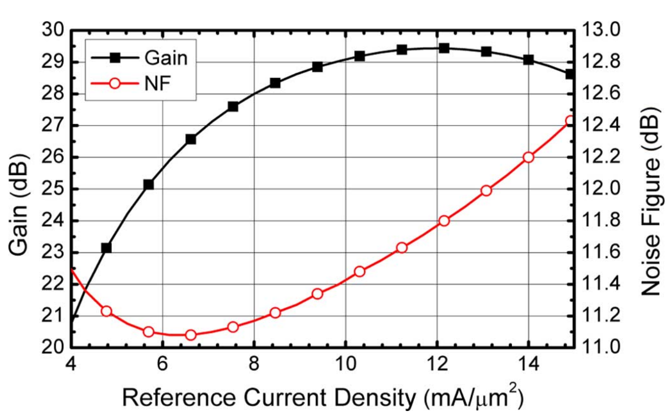

Fig. 8. Simulated gain and noise figure of amplifier B versus collector current density per emitter area at 155 GHz in the BC9MW process.

current density, 6–7 $\mathrm{mA}/\mu\mathrm{m}^2$, is approximately half of that corresponding to the peak gain.

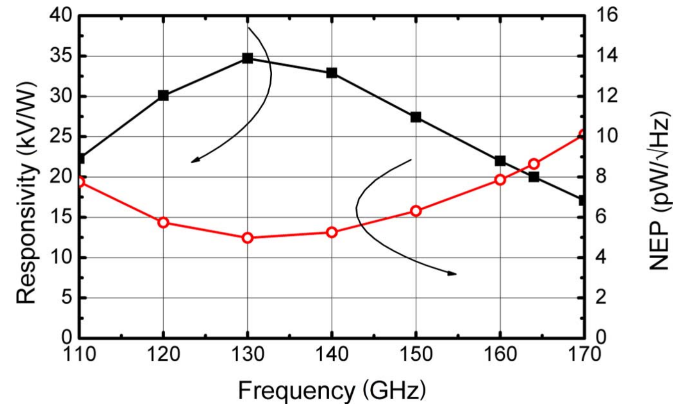

Fig. 9. Simulated responsivity and NEP of the W-band detector (A) as a function of RF input frequency.

C. Detector

The square-law peak detector, shown in Fig. 3, is an HBT adaptation [20] of the nMOS-based version in [12]. It utilizes a differential topology, with single-ended to differential conversion provided by a lumped balun, which also matches the detector input to 50 Ω. The common-mode signal at the emitter of the input transistors $(Q_{1,2})$, which is proportional to the signal amplitude, is amplified by the common-base amplifier formed by transistor Q_5 and the output load resistor. The latter is located off-chip. This arrangement allows for different resistor values and different bias current densities to be experimented with in order to optimize the detector NEP. A dummy reference detector is included on-chip, providing a reference voltage to be used along with the main detector voltage as inputs to a differential (off-chip) post-amplifier. It also helps to suppress power supply noise.

Two detector test structures were fabricated to allow broadband performance testing with reasonably good matching to 50 Ω throughout the W- and D-band. The only difference is the input balun. In version A, suitable for W-band and lower D-band testing, a 3:1 side-coupled structure was employed with a total diameter of 32 μm. Both primary and secondary coils are formed in the top copper layer with $W = 2$ μm and $S = 0.6$ μm. The primary has two coils, while the secondary has a single coil. The inductance of the primary is 122 pH, whereas that of the secondary is 43 pH. Version B, used in the fabricated total power radiometer and targeted at the upper half of the D-band and at the lower G-band, employs a side-coupled 1:1 balun with a single-coil primary and single-coil secondary. It features a metal strip width, $W = 1$ μm, an inter-coil spacing, $S = 0.6$ μm, and a diameter of 24.6 μm. The simulated responsivity and NEP of detector A at the minimum NEP bias is shown in Fig. 9 as a function of frequency. It shows that the NEP is as low as 5 $\mathrm{pW}/\sqrt{\mathrm{Hz}}$ at 130 GHz where the detector input is perfectly matched and that it remains below 10 $\mathrm{pW}/\sqrt{\mathrm{Hz}}$ up to 170 GHz.

III. Fabrication and Process Characterization

The radiometer, amplifier A, and detector breakouts were fabricated along with transistor test structures and on-die thru-reflect-line (TRL) calibration standards in several process splits of a developmental SiGe HBT technology, B4T [5]. Both high-speed, with $\mathrm{BV}_{\mathrm{CEO}}$ of 1.6 V, and medium-voltage, $\mathrm{BV}_{\mathrm{CEO}} >$

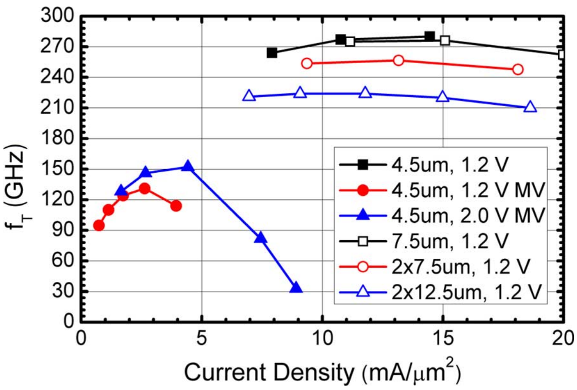

Fig. 10. Measured f_T *versus* J_C characteristics on B4T wafer PGT20 for high-speed and medium-voltage SiGe HBTs biased at $V_{\rm CE} = 1.2$ V and 2 V, respectively.

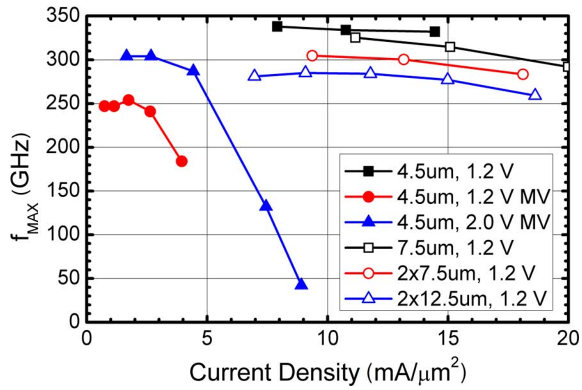

Fig. 11. Measured $f_{\rm MAX}$ *versus* J_C characteristics on B4T wafer PGT20 for high-speed and medium-voltage SiGe HBTs biased at $V_{\rm CE} = 1.2$ V and 2 V, respectively.

2 V, HBTs were fabricated on the same wafer. The BEOL, shown in Fig. 7, is similar to that in [19], with 2-fF/μm^2 MIM capacitors and six copper layers, the top two being 3-μm thick. Several wafers with different B4T process variants were fully characterized. Amplifier A was also fabricated in the BC9MW and B3T processes, whereas amplifier B was fabricated only in the BC9MW process.

S-parameter measurements of transistors, t-lines, transformers, and circuit breakouts were performed with an HP8510C network analyzer interfaced with two D-band OML transmit/receive (T/R) modules and ground–signal–ground (GSG) wafer probes from Cascade Microtech, Beaverton, OR. Both TRL and line-reflect-reflect-match (LRRM) calibrations were performed on standard calibration substrates from GGB, Naples, FL, and Cascade Microtech, without any noticeable differences in the device-under-test (DUT) measurements. The pad and interconnect parasitics of the transistor, t-line, and transformer test-structures were de-embedded using the t-line-based technique described in [21]. In the case of the amplifier, detector and imager measurements, the impact of the pads (approximately 8-fF capacitance) and interconnect is included in all the measured S-parameters. They were not de-embedded.

Figs. 10 and 11 show the measured f_T and $f_{\rm MAX}$ versus current density for high-speed and medium-voltage B4T transistors with 165-nm emitter width and various emitter lengths. As illustrated in Fig. 12, the metallization on top of the transistor, up to and including metal 6, was not removed by de-embedding in order to capture the true circuit performance of the transistor. f_T and $f_{\rm MAX}$ were extrapolated from the measured $20\log_{10}|H_{21}(f)|$ and $10\log_{10}(U(f))$ characteristics, averaged in the 110–125-GHz range where the slope versus frequency is approximately 20 dB/decade.

As can be seen in Figs. 10 and 11, for very large emitter lengths, the interconnect series resistance and parasitic capacitance start to degrade f_T and $f_{\rm MAX}$. It is also important to note that $f_{\rm MAX}$ of the medium-voltage HBTs is almost as large as that of the high-speed HBTs at about 1/3 of the current density, whereas f_T is reduced to half.

For comparison with the performance of the other two SiGe HBT processes, the measured MAG at 120 GHz of representative high-speed B4T, B3T, and BC9MW HBTs, is reproduced

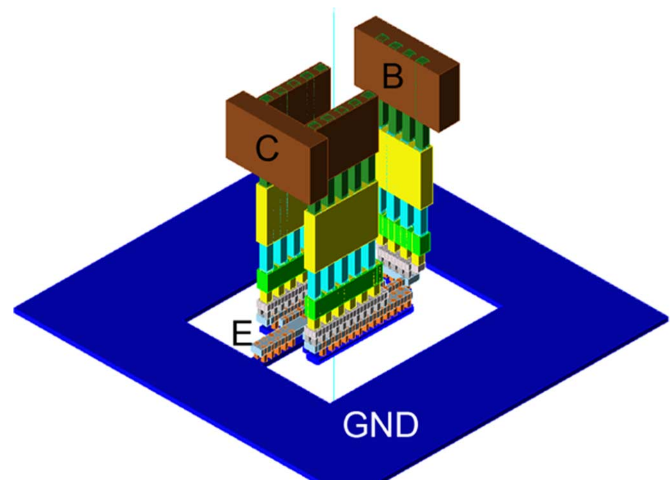

Fig. 12. Transistor with metallization, after de-embedding pad and interconnect parasitics [20].

in Fig. 13. It can be observed that the peak MAG ($f_{\rm MAX}$) current density remains approximately the same between the three processes while MAG (hence, $f_{\rm MAX}$) improves by almost 3 dB from BC9MW to B4T. Additionally, the f_T and $f_{\rm MAX}$ characteristics measured on a high-speed 0.165 μm × 4.5 μm SiGe HBT across different B4T process splits are compiled in Figs. 14 and 15, respectively. Note that f_T and $f_{\rm MAX}$ vary by 10%–15% across splits.

IV. Circuit Breakout Characterization

A. Amplifier Performance

The die photographs of amplifiers A and B are shown in Figs. 16 and 17, respectively.

Fig. 18 shows the measured S_{21} of type A amplifiers for three different HBT vertical profiles (BC9MW, B3T, and B4T). Additionally, two versions each of the BC9MW and B3T amplifiers with 130- and 120-nm emitter widths are included. The impact of reducing emitter width on BC9MW amplifiers is almost as high as changing the vertical HBT profile from BC9MW to B3T. The peak amplifier gain shifts in frequency from 156 to 163 GHz and increases from 18 to 24 dB, whereas the change in profile from BC9MW to B3T at the same emitter width causes a 8-dB increase in peak gain and a shift to 163 GHz. The overall improvement in gain between BC9MW

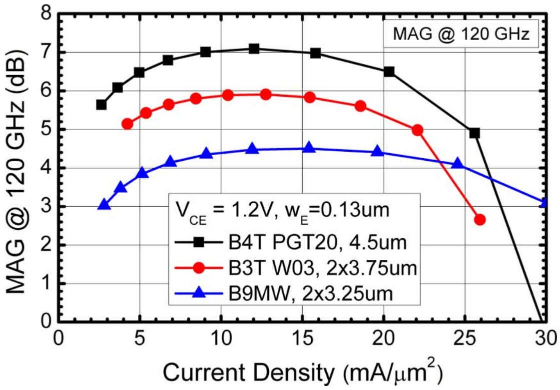

Fig. 13. Measured SiGe HBT MAG @ 120 GHz versus J_C characteristics at $V_{\rm CE} = 1.2$ V for BC9MW, B3T, and B4T process variants.

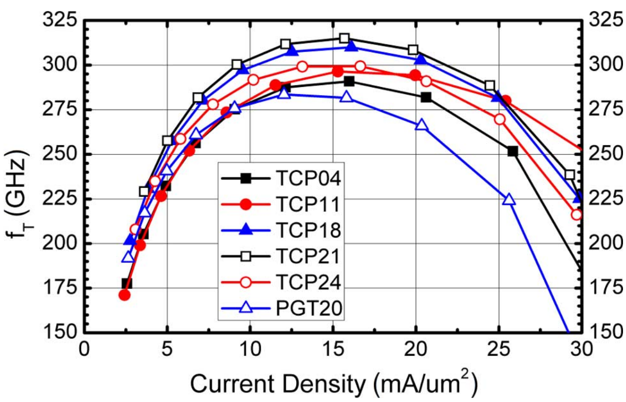

Fig. 14. Measured 0.165 μm $\times$ 4.5 μm SiGe HBT f_T versus J_C characteristics over B4T process splits at $V_{\rm CE} = 1.2$ V.

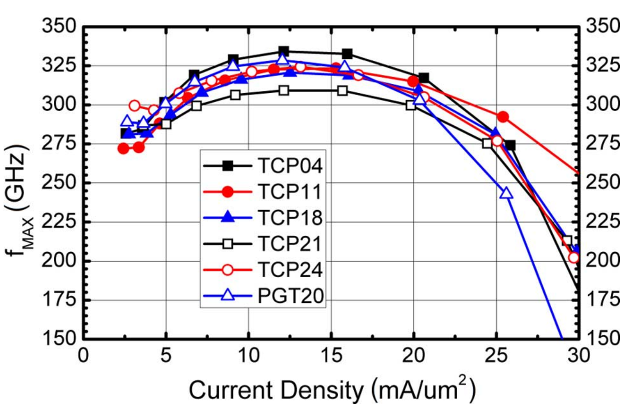

Fig. 15. 0.165 μm $\times$ 4.5 μm SiGe HBT $f_{\rm MAX}$ versus J_C characteristics over B4T process splits at $V_{\rm CE} = 1.2$ V.

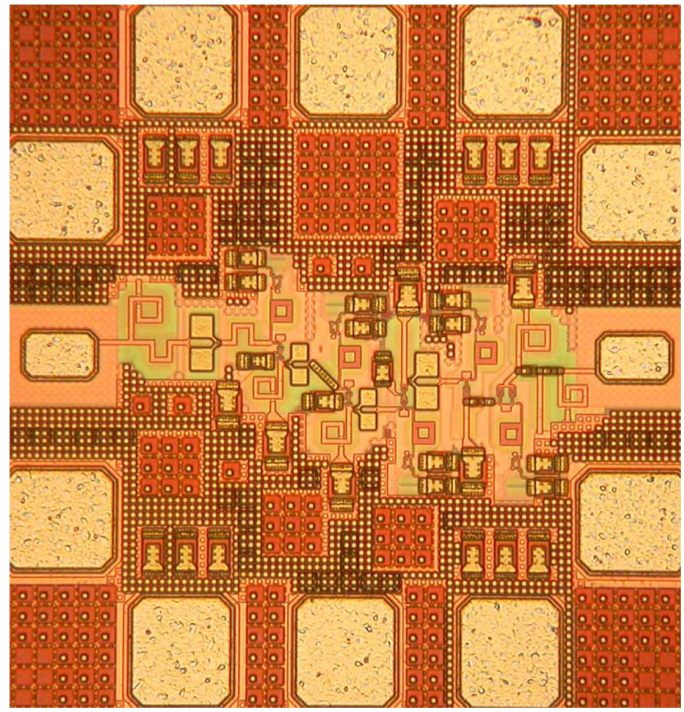

Fig. 16. Die photograph of amplifier A showing the inductor- and capacitor-based matching networks.

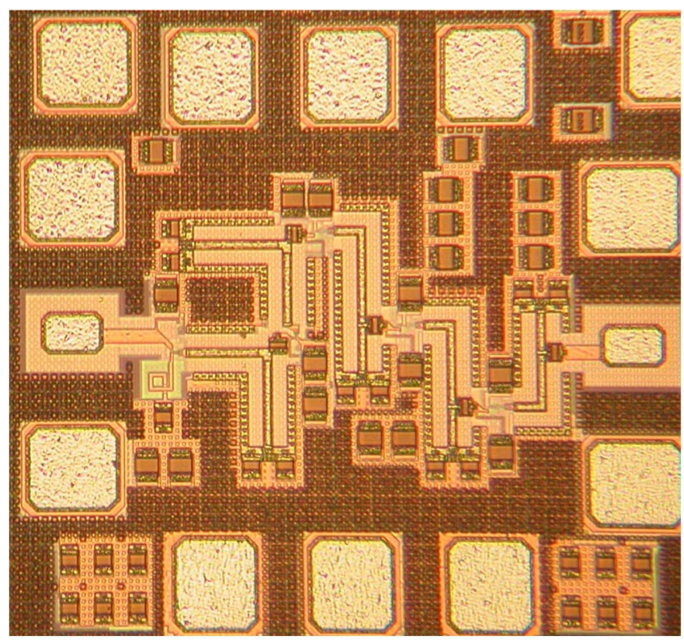

Fig. 17. Die photograph of amplifier B showing the t-line matching networks and single degeneration inductor in the first stage.

and B4T is about 18 dB, spread across three cascode and two CE stages. This is consistent with the 2.5–3-dB improvement in HBT MAG seen in Fig. 13 and the much higher simulated gain of the cascode versus the CE stage in Fig. 4.

Fig. 19 compares the measured S-parameters of amplifiers A and B fabricated in the BC9MW process. The gain of amplifier B peaks at 185 GHz to 22 dB when the last three stages are biased at half the peak-f_T current density. The S-parameters of amplifier A were mapped across B4T process splits. The measured S_{21} at peak-f_T bias current density and at half peak-f_T bias current density in the cascode stages is reproduced in Figs. 20 and 21, respectively. In both cases, wafer PGT20 has the highest amplifier gains. Interestingly, of all the tested B4T wafers, this wafer has the lowest f_T, but the second best $f_{\rm MAX}$, within 1 GHz of the best $f_{\rm MAX}$ value. This trend agrees very well with that observed for a 140-GHz amplifier in a earlier generation, pre-BC9MW, of an SiGe HBT process [22].

B. Detector Performance

The detector breakout die photograph is reproduced in Fig. 22. The responsivity and NEP [20] of the two standalone

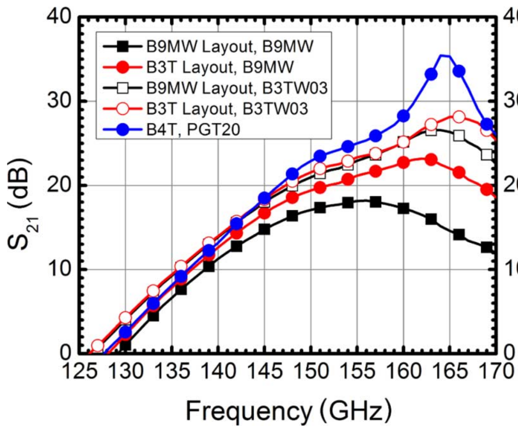

Fig. 18. Impact of HBT vertical profile and and emitter width on the measured amplifier S_{21}.

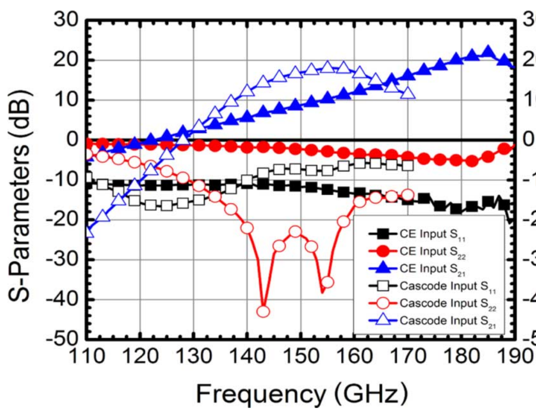

Fig. 19. Comparison of the measured S-parameters of BC9MW cascode-input and CE-input amplifies centered at 165 and 185 GHz, respectively.

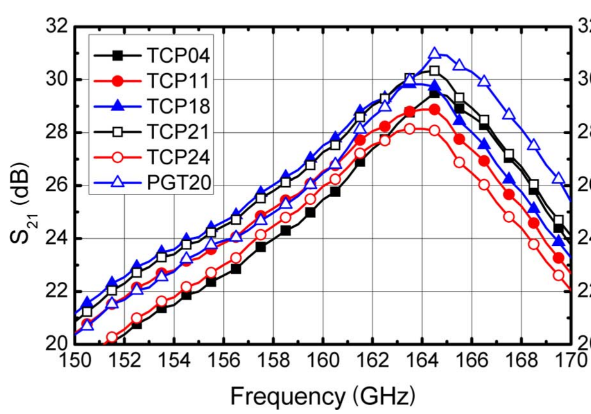

Fig. 20. Comparison of the measured S_{21} of amplifier A across B4T wafer splits when the HBTs in the cascode stages are biased at peak f_T.

detectors were measured as a function of RF frequency and bias current density using the setup in Fig. 23. The output noise spectra were recorded with a spectrum analyzer. Simultaneously, the dc output voltage was measured with a multimeter [12] at a known signal source power and with the signal source turned off. The gain of the postamplifier was de-embedded from all responsivity and NEP measurements. The responsivity and NEP were determined as

$$R = \frac{V_{o\mathrm{DC}}(P_{\mathrm{in}}) - V_{o\mathrm{DC}}(0)}{P_{\mathrm{in}}} \tag{3}$$

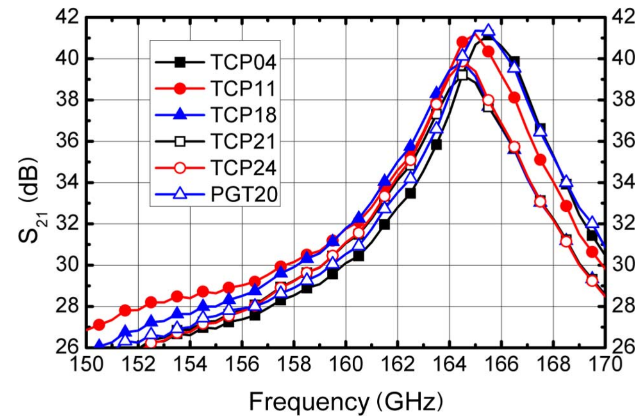

Fig. 21. Comparison of the measured S_{21} of amplifier A across B4T wafer splits when the HBTs in the cascode stages are biased at half the peak-f_T current density.

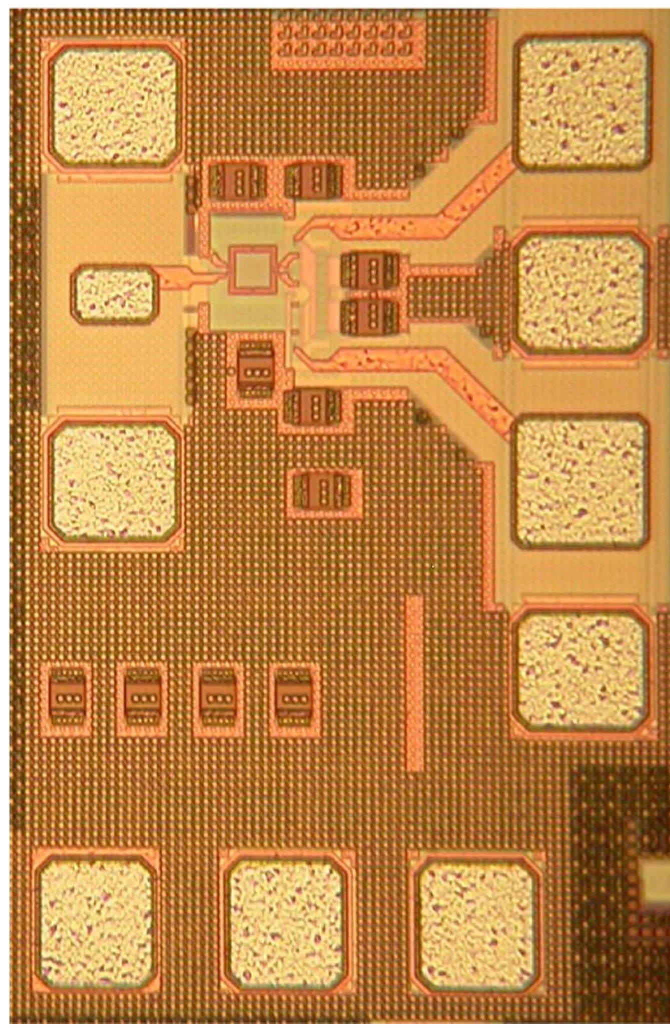

Fig. 22. Die photograph of detector breakout B.

$$\mathrm{NEP}(f_m) = \frac{v_{no}(f_m)}{R} \tag{4}$$

respectively, where P_{in} is the known input signal source power chosen to ensure that the detector operates in linear mode and

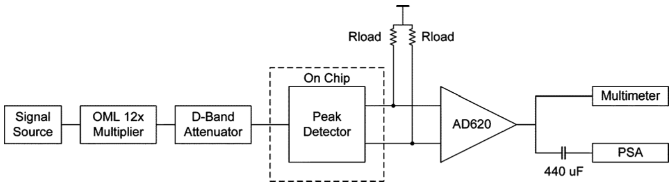

Fig. 23. Measurement setup for detector responsivity and NEP.

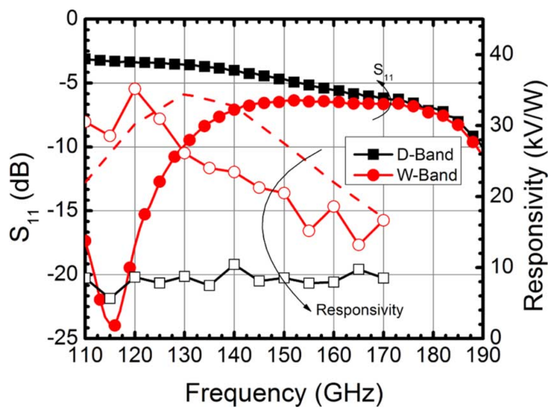

Fig. 24. Measured S_{11} and responsivity of the two detector breakouts on wafer TCP11 for 10-kΩ load resistors and a detector current density of 0.35 mA/μm^2. The simulated responsivity of detector A (W-band) is also shown with dashed lines.

$v_{no}(f_m)$ is the output noise voltage in V/$\sqrt{}$Hz at the dc offset frequency f_m,

Fig. 24 shows the measured S_{11} and responsivity of the two detector breakouts and the simulated responsivity of detector A, as a reference. The larger, 3:1 balun provides good matching to 50 Ω at W-band and up to about 130 GHz for the real part of the input impedance of the detector, which is approximately 20 Ω. The smaller 1:1 balun tunes out the imaginary part of the detector at 190 GHz. In the radiometer, this resonance moves down in frequency due to the output capacitance of the LNA. This is the reason why the 1:1 transformer, rather than the 3:1 version, was employed in the radiometer. The peak responsivity of the W-band detector corresponds to the frequency at which S_{11} reaches its optimum. In fact, the responsivity of the two detectors closely tracks their S_{11} variation across the D-band with the two detector breakouts exhibiting almost identical responsivity and S_{11} in the 160–170-GHz range.

The NEP is plotted in Fig. 25 as a function of RF frequency for two different load resistor values of 1 and 10 kΩ, respectively. These measurements were taken at the minimum NEP current density of 0.35 mA/μm^2 at dc offset frequency of 1 kHz, beyond the $1/f$ noise corner [19]. Although the responsivity of the detector is ten times larger when a 10-kΩ load is employed, the NEP improves only by a factor of 1.5 to 2. Ideally, if the load resistor was noiseless, the NEP should not depend on the load resistor value. However, the load resistor itself contributed to the overall detector NEP. Its noise must be minimized by selecting a large enough resistor value and a resistor that has very low $1/f$ noise. Note that simulations overestimate the NEP of the detector. This is similar to the overestimation of amplifier noise

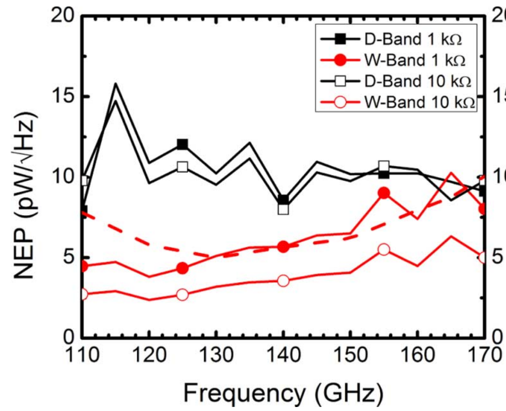

Fig. 25. Measured NEP at 1-kHz offset as a function of RF frequency for both detectors on wafer TPC11 for 1- and 10-kΩ load resistors and a detector current density of 0.35 mA/μm^2. Simulation results for 10-kΩ load resistor are also shown for comparison.

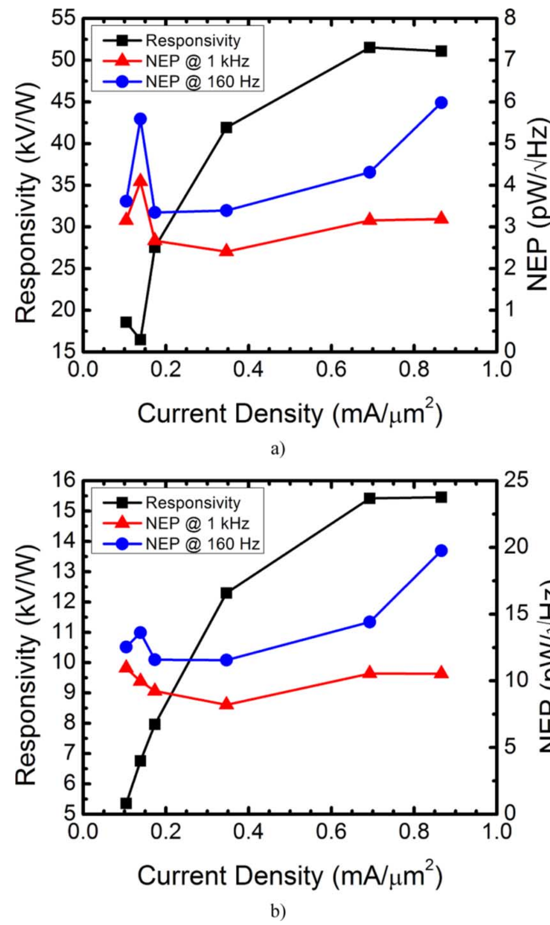

Fig. 26. Comparison of the measured responsivity and NEP of the W-band detector breakout A on wafer TCP11 for 10-kΩ load resistors at: (a) 120 and (b) 165 GHz as a function of current density at offset frequencies of 160 Hz and 1 kHz, respectively.

figure and voltage-controlled oscillator (VCO) phase noise observed with this HBT model.

As illustrated in Fig. 26, the optimal current density reduces to 0.175 mA/μm^2 when the NEP is measured at a dc offset frequency of 160 Hz.

The NEP and responsivity measurements were repeated for several supply voltages on the load resistor and they were found to be largely constant for dc voltages at the load resistor output

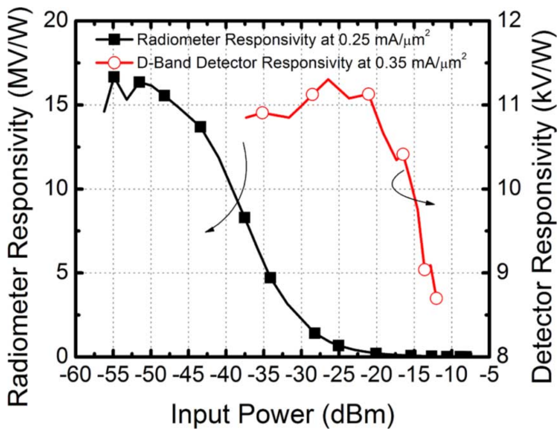

Fig. 27. Measured responsivity at 165 GHz for the D-band detector on wafer TCP11 biased at 0.35 mA/μm^2 and for the radiometer as a function of input power when the detector is biased at 0.25 mA/μm^2.

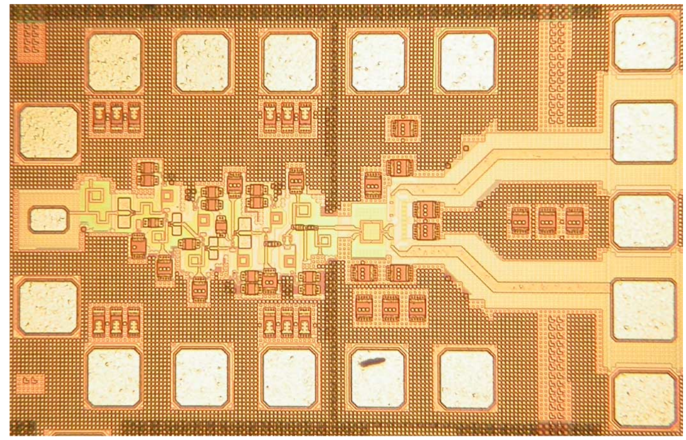

Fig. 28. Die photograph of the radiometer, including LNA and detector. The dimensions are 765 $\times$ 490 μm^2.

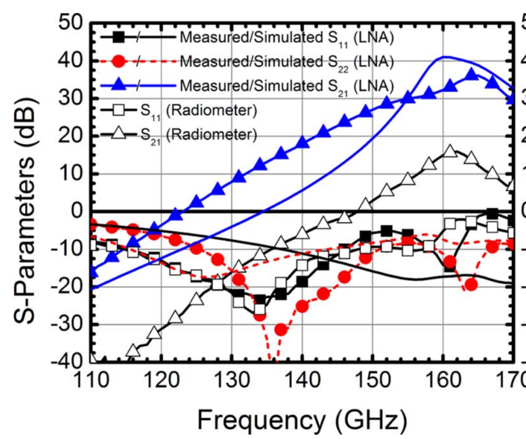

Fig. 29. S-parameters (lines and symbols) and responsivity of the radiometer and of the standalone LNA measured on B4T wafer TCP11. Simulation results for the LNA S-parameters are also shown with lines only.

of 1.1–2.4 V. The detector input return loss, responsivity, and NEP measurements reveal the importance of S_{11} on detector and radiometer performance and that lumped transformers can be used in silicon millimeter-wave integrated circuits (ICs), even at 190 GHz. Furthermore, the most important detector figure of merit, the NEP and its optimal bias conditions, are closely related to the $1/f$ noise of the HBT and to the bias current at which the HBT $1/f$ noise, the $1/f$ noise corner, and the HBT noise above the $1/f$ corner are simultaneously reduced [19]. The detector responsivity plays a secondary role compared to its NEP since the responsivity can always be boosted by using larger load resistors and/or low-noise post amplifiers. At the optimal bias that minimizes the NEP at 160-Hz offset, the standalone detector consumes 1.7 mW from 1.2- and 2.1-V power supplies.

Fig. 27 reproduces the measured responsivity of the D-band detector as a function of input power at 165 GHz when the detector is biased at a current density of 0.35 mA/μm^2. The detector is linear below -20 dBm and begins to saturate at higher input levels. It was not possible to determine at what power level the responsivity decreases by a factor of 2 due to the limited output power of the signal source available in the D-band. For comparison, the measured responsivity of the entire radiometer, larger than 17 MV/W at a lower bias current density in the detector, is also shown. The 1-dB input compression point of the radiometer responsivity is smaller than -50 dBm.

V. Radiometer Characterization

A die photograph of the radiometer is reproduced in Fig. 28. The circuit occupies an area of 765 $\times$ 490 μm^2 and is pad limited. Fig. 29 reproduces the measured S-parameters of the radiometer and of the standalone LNA, measured on the same wafer, TCP11, and under identical bias conditions. The simulated S-parameters of the LNA are also shown for comparison. Even when the LNA cascode stages are biased at the peak-f_T current density, the S_{11} of the radiometer remains below -6 dB throughout the frequency range. The radiometer S_{21}, measured between the radiometer input and one of the detector outputs, peaks at 161 GHz, coinciding with the peak in the measured responsivity of the radiometer.

Direct NETD measurements were performed in the setup shown in Fig. 30, using a calibrated D-band ELVA-1 solid-state noise source with a 13-dB excess noise ratio (ENR). The D-band waveguide attenuator placed after the noise source permitted controlling the input noise power level reaching the DUT. The calibrated noise source was switched between the hot and cold states via an external modulation voltage. The cold noise state is approximately equal to the ambient room temperature of 290 K, and the hot noise state is approximately 13 dB above this, or 6076 K. The radiometer output voltage difference between the hot and cold states was measured using a multimeter, and the output noise spectra at baseband were simultaneously monitored using a spectrum analyzer. To facilitate measurements in a 50-Ω environment, and to amplify the radiometer output signal above the noise floor of the test equipment, an off-chip low-noise post-amplifier was used (AD620), but its gain was de-embedded from all measurement results.

The expressions of the responsivity and of the NEDT are given by

$$R = \frac{V_{o\mathrm{DC}}}{N_{\mathrm{inRF}}} \tag{5}$$

This article has been accepted for inclusion in a future issue of this journal. Content is final as presented, with the exception of pagination.

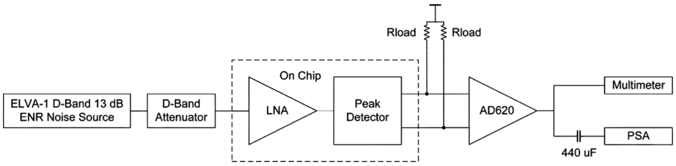

Fig. 30. Radiometer test setup with calibrated solid-state noise source.

and [10]

$$\mathrm{NEDT} = \frac{\mathrm{NEP}}{k\Delta f_{\mathrm{RF}}\sqrt{2\tau}} \tag{6}$$

respectively, where $V_{o\mathrm{DC}}$ is the measured output dc voltage corresponding to N_{inRF}, the input noise-power generated by the noise source in the hot state

$$N_{\mathrm{inRF}} = kT\Delta f_{\mathrm{RF}} 10^{(\mathrm{ENR_{dB}} - \mathrm{RF_{loss}})/10} \tag{7}$$

where $\mathrm{RF_{loss}}$ describes the input setup loss between the noise source and the DUT. NEP is obtained from the measured output noise voltage at dc offset frequency $\mathbf{f_m} = 1/2\tau$, normalized to $1\sqrt{\mathrm{Hz}}$,

$$\mathrm{NEP} = \frac{v_{no}}{R} = \frac{\frac{v_{no}}{V_{o\mathrm{DC}}}}{N_{\mathrm{inRF}}} \tag{8}$$

By plugging (8) and (7) into (6), the final expression for NEDT is then recast as

$$\mathrm{NEDT} = \frac{v_{no}}{k\sqrt{2\tau}V_{o\mathrm{DC}}} 10^{(-204+\mathrm{ENR}-\mathrm{RF_{LOSS}})/10} \tag{9}$$

where -204 is the ambient-temperature noise-floor (dBW), integrated over 1-Hz bandwidth in watts. Thus, with a known ENR (manufacturer provided), $\mathrm{RF_{LOSS}}$ (measured independently), and a given integration time (system-implementation specific), the temperature resolution depends on the measured output noise voltage at $1/2\tau$ and the measured dc voltage change between the hot and cold noise states of the calibrated noise source. Note that, with this NETD measurement method, the RF noise bandwidth need not be known since it cancels out and does not appear in the NETD (9).

The measured output noise voltage spectra of the radiometer are reproduced in Figs. 31 and 32 for two different bias conditions of the LNA and of the detector. Both the hot (top) and the cold (middle) noise spectra are shown, along with the output noise spectra when the LNA is unbiased, shown in the bottom trace as a reference. A $1/f$ noise corner of approximately 500 Hz can be observed, with the low-frequency noise being dominated by 60-Hz harmonic tones. For the spectrum in the middle, the $1/f$ noise corner is less than 200 Hz, while no $1/f$ noise can be observed for the top spectrum when the noise source is in the hot state. The signal roll-off at very low-frequencies (<20 Hz) is caused by the dc blocking capacitor required in front of the PSA. Both the output noise level and the $1/f$ noise corner of the detector are reduced under the bias conditions in Fig. 32 when the LNA supplies are 1.4 and 2.8 V and the bias current density in the detector is set to $0.175\ \mathrm{mA}/\mu\mathrm{m}^2$.

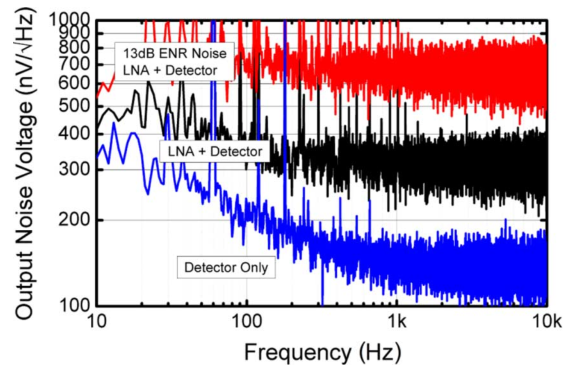

Fig. 31. Measured radiometer output noise on-wafer PGT20 with hot noise source (*top*), cold noise source, and with the LNA bias turned off and cold noise source (*bottom*). The LNA stages are biased at the peak-f_T current density from 1.5- and 3-V supplies and the detector is biased at $0.25\ \mathrm{mA}/\mu\mathrm{m}^2$, corresponding to the minimum detector NEP at 1-kHz offset.

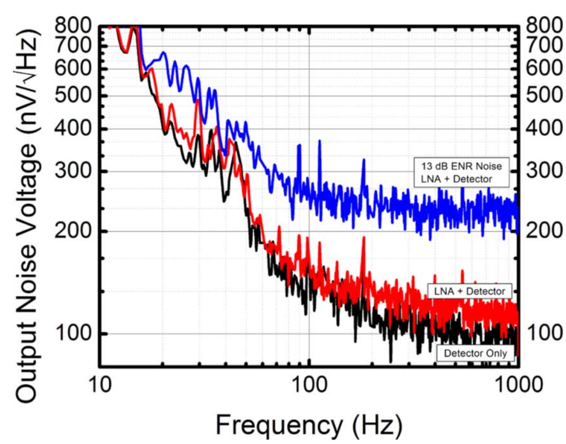

Fig. 32. Measured radiometer output noise on wafer TCP11 with hot noise source (*top*), cold noise source, and with the LNA bias turned off and cold noise source (*bottom*). The LNA stages are biased at the half-peak-f_T current density from 1.4- and 2.8-V supplies and the detector is biased at $0.175\ \mathrm{mA}/\mu\mathrm{m}^2$, corresponding to the minimum detector NEP at 160 Hz.

The NEDT was measured for a variety of bias conditions using the cold-state noise voltage at $1/2\tau = 160$ Hz and the hot-state output dc voltage change. As can be concluded from the output noise spectra in Figs. 31 and 32, it is critical to optimally bias the LNA for high gain and low noise, and the detector for minimum $1/f$ noise, both important contributors to the noise performance and the NEDT of the radiometer.

Fig. 33 shows the measured NEDT, at a low-frequency offset of 160 Hz, and the radiometer responsivity as a function of the current density in the input stage of the LNA. Since the minimum noise figure current density of the HBT cascode is different from the peak gain bias, the optimal bias setting differs for responsivity (optimized by peak gain) and NEDT (optimized by minimal noise). These results were obtained assuming an integration time of 3.125 ms, as in [4], a measured input system loss of 4.15 dB, and by averaging the measured output noise voltage between 150–170 Hz. A minimum temperature resolution of approximately 0.35 K is observed. When biased for optimal noise performance, the LNA consumes 36 mA from 1.4 V and 13 mA from 2.8 V, for a total of 92 mW, including the bias current mirrors.

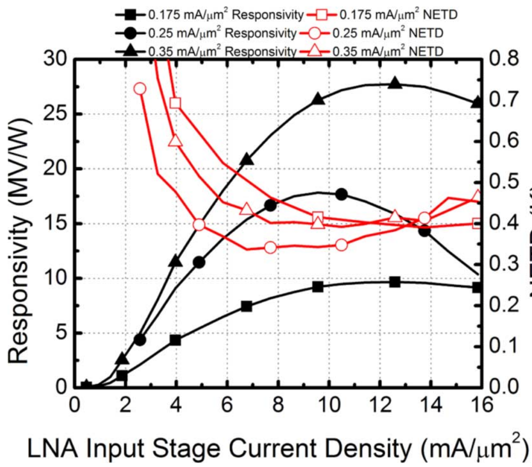

Fig. 33. Measured NEDT on wafer TCP11, at 160-Hz offset, and output dc voltage change as a function of the LNA input stage current density with the detector biased at 0.175 and 0.35 mA/μm^2, using 1.4- and 2.8-V supplies on the LNA, and with the detector biased at 0.25 mA/μm^2, using 1.5- and 3.1-V supplies on the LNA.

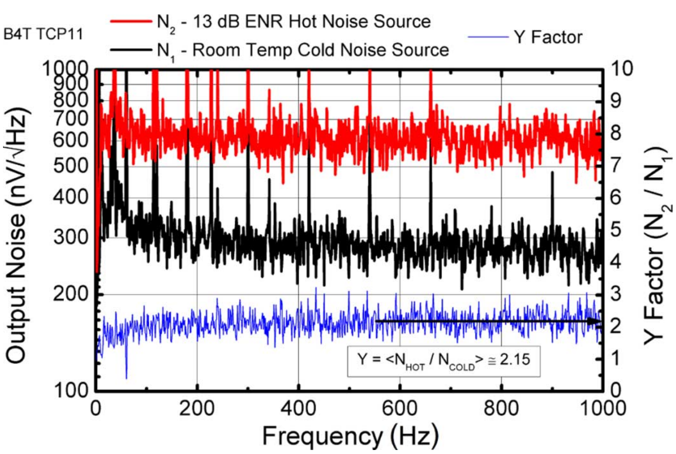

Fig. 34. Measured output noise spectra for hot and cold states and the corresponding Y-factor.

When the detector was biased at 0.175 mA/μm^2, which reduces the detector NEP at 160-Hz offset, the radiometer measurements show approximately the same NETD as when the detector was biased at 0.35 mA/μm^2. This is despite the fact that the radiometer responsivity decreases 2.8 times. However, the minimum NETD now occurs at a higher LNA input current density. This implies that the LNA has insufficient gain to suppress the detector noise above 300 Hz, but also that the radiometer exhibits lower overall output noise at 160-Hz offset. These results agree with the findings in [4] for a W-band InP radiometer where the $1/f$ noise of the detector was found to have greater impact than the LNA gain and noise figure in the NETD of the radiometer.

The system noise figure and noise temperature—averaged over the system noise bandwidth—can be determined by observing the ratio of the noise-power between the hot and cold noise states, in a manner similar to the traditional Y-factor noise figure measurement technique. Fig. 34 reproduces the hot and cold noise spectra for the radiometer (top and middle curves) with the noise-power ratio (Y-factor) shown in the bottom curve. The ratio of the two powers is averaged between

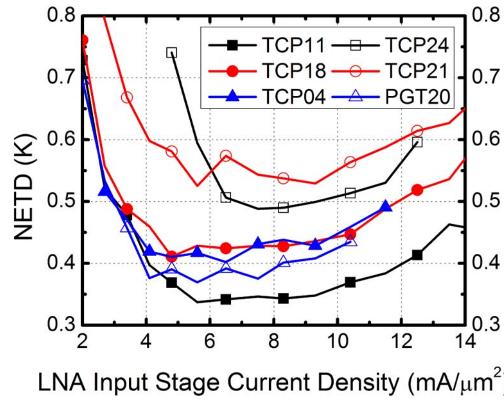

Fig. 35. Measured NEDT (from the output noise spectra at 160-Hz offset corresponding to $\tau = 3.125$ ms) across process splits as a function of the LNA input stage current density. The LNA supplies were 1.5 and 3 V.

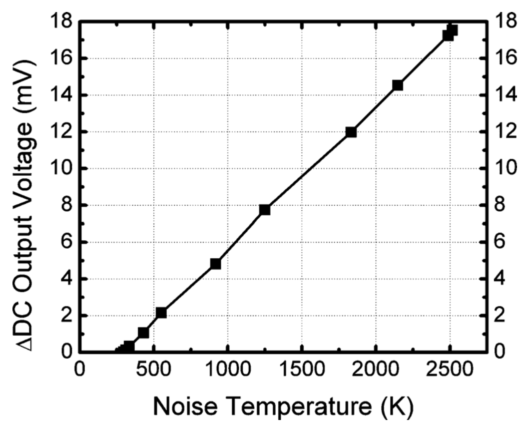

Fig. 36. Measured output dc voltage change as a function of input noise temperature on wafer TCP11, with the detector biased at 0.35 mA/μm^2 and using 1.4- and 2.8-V supplies on the LNA.

300 Hz–1 kHz. An average Y-factor of 2.15 is measured, which corresponds to an average system noise figure of

$$\mathrm{NF_{SYS}} = \mathrm{ENR} - 10\log_{10}(Y-1) = 12.4 \text{ dB}$$

When subtracting the 4.15-dB setup loss at the input, an average system noise figure of 8.25 dB is obtained. A system noise temperature of 1645 K can be also derived from the average noise factor and from the noise bandwidth. The latter is bias dependent, rather ambiguous, and can be calculated from the measured radiometer $S_{21}(f)$ characteristics in Fig. 29

$$\Delta f_{\mathrm{RF}} = \frac{\left[\int\limits_{110\mathrm{GHz}}^{170\mathrm{GHz}} S_{21}(f)df\right]^2}{\int\limits_{110\mathrm{GHz}}^{170\mathrm{GHz}} S_{21}^2(f)df} \approx 10\text{–}16 \text{ GHz} \tag{10}$$

or can be approximated by multiplying the 3-dB bandwidth with $\pi/2$.

The NETD of the radiometer was mapped across the B4T wafer splits and plotted in Fig. 35 against the collector current density of the input transistor of the LNA. In general, the best NEDT is obtained on the wafers that also have the highest amplifier gain: TCP11 and PGT20. Note also that the optimum NETD current density is higher for wafer TCP11 than for wafer

TABLE I
COMPARISON OF TOTAL POWER RADIOMETER PERFORMANCE

Reference	InP [4]	SiGe [10]	SiGe [11]	CMOS[12]	Bolometer [1]	This work
f (GHz)	94	94	90	90	0.2 – 1 THz	165
Δf_{RF} (GHz)	28	20	26	18	800 GHz	10
T_{SYS} (K)	750		4306			1645
NEP ($fW/Hz^{1/2}$)	0.9	23	35	36	8 @7 K	14-19
R (MV/W)	4.5	2.5	43	0.67		28
NETD (K) @ freq offset τ	0.29 @ 3.125 mS	0.69 @10 kHz 30 ms	0.4 @? 30 ms	0.55 @ 400 kHz 30 ms	0.54 @6-30 Hz 0.725 ms	0.35 @160 Hz, 3.125 mS
P_{DC} (mW)	?	34.8	200	110	15000/channel	95
LNA gain (dB)	30-35	24	30	36	-	>35
Det.NEP ($pW/Hz^{1/2}$)	1	4	NF = 39 dB	200	0.008 @7 K 10 @ 290 K	<6 at D-Band <2.5 at W-Band
Det. R (kV/W)	15	12	12	0.2		11
Det. 1/f corner (Hz)	1000	10000	NA	>1 MHz	30	<500

PGT20, in agreement with the HBT peak-f_T current density in Fig. 14. The spread in NETD across wafer splits is 2–3 dB (from 0.35 to 0.55 K).

The preceding measurement setup and the experimental results collected using it demonstrate that the most important figures of merit of the radiometer, its sensitivity and system noise temperature can be determined solely with low-frequency instrumentation and a relatively low-cost D-band noise source. No millimeter-wave measurements are required, thus minimizing large volume production test cost.

In contrast, to determine the radiometer responsivity, a D-band signal source and power measurements are required.

From the measured responsivity of 9.6 MV/W in Fig. 33 and from the output noise voltage of 136 nV/$\sqrt{}$Hz in Fig. 32, a minimum radiometer NEP of 14 fW/$\sqrt{}$Hz is obtained on wafer TCP11 at a detector current density of 0.175 mA/μm^2. From the measured responsivity of 17 MV/W in Fig. 33 and from the output noise voltage of 320 nV/$\sqrt{}$Hz in Fig. 31, a minimum radiometer NEP of 19 fW/$\sqrt{}$Hz is obtained at a detector current density of 0.25 mA/μm^2.

It should be noted that the radiometer occupies a much smaller area than the heterodyne receiver in [16], making it ideally suitable as a process monitor for the 50-Ω noise measure of the HBT and/or cascode stage using low-frequency test equipment and a D-band noise source.

Finally, a measurement of dc output voltage as a function of the input noise power was performed to quantify the thermal sensitivity of the radiometer. The results shown in Fig. 36 correspond to a thermal sensitivity of 8 μV/K, higher than that in [9]. This plot was obtained by changing the temperature of the D-band noise source using a variable attenuator.

Table I compares the performance of this radiometer with other passive imaging receivers fabricated in CMOS, SiGe, and III–V technologies. The NETD, integration time, and to a less extent the RF bandwidth, depend on system architecture and implementation choices rather than transistor and detector technology.

VI. CONCLUSION

An integrated D-band radiometer with pre-amplification has been demonstrated in a developmental SiGe HBT technology. Wafer mapping across several process splits indicates that the best radiometer sensitivity is obtained on the wafers with highest SiGe HBT f_{MAX}, which result in the highest LNA gain. If the LNA gain is sufficient to overcome the detector noise, typically over 40 dB), then the optimum LNA bias current density for best radiometer sensitivity corresponds to the minimum noise figure/noise measure current density of the input LNA stage. To these authors' knowledge, this marks the first D-band total power radiometer integrated in any semiconductor technology. Its performance is comparable or better than that of published W-band radiometer in silicon. The system consumes 95 mW and occupies 765 $\times$ 490 μm^2. Temperature resolution and NEP values as low as 0.35 K and 14 fW/Hz$^{1/2}$, respectively, estimated using standard 3.125-ms integration times and the measured noise spectra at 160 Hz, indicate the possibility of using such a system without any form of noise chopping due to the excellent $1/f$ noise corner, below 200 Hz. The very low $1/f$ noise corner of the radiometer appears to indicate that, unlike InP HEMT LNAs, high-gain SiGe HBT LNAs do not suffer from gain fluctuations.

The state-of-the radiometer results and the large gain amplifiers at 165 and 185 GHz reported in this paper suggest that the D-band could emerge as a sweet spot for silicon-based imaging. In comparison with the W-band, it benefits from several key advantages, including: 1) simpler and more efficient on-die antenna integration; 2) potential for wider-bandwidth systems; 3) smaller form factor; and 4) lower power consumption per pixel. At the same time, SiGe BiCMOS technology is ideal for the fabrication of total power radiometers since it features lower $1/f$ noise corner than both CMOS and III–V technologies, larger gain per bias current consumption, and better BEOL than nanoscale CMOS at a comparable price. Although wafer-scale integration of a 2-D pixel array in SiGe BiCMOS or sub 32-nm

CMOS technologies is attractive, market volumes need to increase significantly to justify the development cost.

ACKNOWLEDGMENT

The authors would like to thank J. Pristupa, University of Toronto, Toronto, ON, Canada, and CMC Microstystems, Kingston, ON, Canada, for computer-aided design (CAD) support and the National Science and Engineering Research Council (NSERC) of Canada, Ontario Innovation Trust (OIT), and Canada Foundation for Innovation (CFI) for equipment grants.

The authors also thank STMicroelectronics, Crolles, France, for donating the chips used in this study.

REFERENCES

[1] A. Luukkanen, "Passive and active submm-wave imaging for stand-off security screening applications," presented at the IEEE MTT-S Int. Microw. Symp. WSC Imag. Workshop, Jun. 2011.

[2] P. Kangaslahti, D. Pukala, D. Hoppe, A. Tanner, T. Gaier, and B. Lambrigtsen, "Broadband millimeter wave receiver with dual polarization," in *IEEE MTT-S Int. Microw. Symp. Dig.*, Jun. 2011, Paper WE1G-1.

[3] A. Tang and F. Chang, "Advantages of the CMOS receiver for millimeter and sub-millimeter wave imaging," presented at the IEEE MTT-S Int. Microw. Symp. WSC Imag. Workshop, Jun. 2011.

[4] J. J. Lynch, "W-band sensors fopr passive millimeter wave imaging," presented at the IEEE MTT-S Int. Microw. Symp. WSC Imag. Workshop, Jun. 2011.

[5] A. Chantre *et al.*, "Pushing conventional SiGe HBT technology towards "Dotfive" terahertz," in *Eur. Microw. Integr. Circuits Conf.*, 2010, pp. 21–24.

[6] Y. A. Atesal, B. Cetinoneri, M. Chang, R. Alhalabi, and G. M. Rebeiz, "Millimeter-wave wafer-scale silicon BiCMOS power amplifiers using free-space power combining," *IEEE Trans. Microw. Theory Tech.*, vol. 59, no. 4, pp. 954–965, Apr. 2011.

[7] I. Sarkas, J. Hasch, A. Balteanu, and S. Voinigescu, "A fundamental frequency, single-chip 120-GHz SiGe BiCMOS precision distance sensor with above IC antenna operating over several meters," *IEEE Trans. Microw. Theory Tech.*, submitted for publication.

[8] A. Pergande, "The history and challenges of passive millimeter wave imaging," presented at the IEEE MTT-S Int. Microw. Symp. WSC Imag. Workshop, Jun. 2011.

[9] J. J. Lynch *et al.*, "Passive millimeter-wave imaging module with preamplified zero-bias detection," *IEEE Trans. Microw. Theory Tech.*, vol. 56, no. 7, pp. 1592–1600, Jul. 2008.

[10] J. W. May and G. M. Rebeiz, "Design and characterization of W-band SiGe RFICs for passive millimeter-wave imaging," *IEEE Trans. Microw. Theory Tech.*, vol. 58, no. 5, pp. 1420–1430, May 2010.

[11] L. Gilreath, V Jain, H.-C. Yao, L. Zheng, and P. Heydari, "A 94-GHz passive imaging receiver using a balanced LNA with embedded Dicke switch," in *IEEE Radio Freq. Integr. Circuits Symp.*, 2010, pp. 79–82.

[12] A. Tomkins, P. Garcia, and S. P. Voinigescu, "A passive W-band imager in 65 nm bulk CMOS," *IEEE J. Solid-State Circuits*, vol. 45, no. 10, pp. 1981–1991, Oct. 2010.

[13] S. Koch, M. Guthoerl, I. Kallfass, A. Leuther, and S. Saito, "A 120–145 GHz heterodyne receiver chipset utilizing the 140 GHz atmospheric window for passive millimeter-wave imaging applications," *IEEE J. Solid-State Circuits*, vol. 45, no. 10, pp. 1961–1967, Oct. 2010.

[14] H. Zirath *et al.*, "Integrated receivers up to 220 GHz utilizing GaAs-mHEMT technology," in *IEEE RFIT*, 2009, pp. 225–228.

[15] E. Laskin, P. Chevalier, B. Sautreuil, and S. P. Voinigescu, "A 140-GHz double-sideband transceiver with amplitude and frequency modulation operating over a few meters," in *IEEE BCTM Dig.*, 2009, pp. 178–181.

[16] K. H. K. Yau, P. Chevalier, A. Chantre, and S. P. Voinigescu, "Characterization of the noise parameters of SiGe HBTs in the 70–170 GHz range," *IEEE Trans. Microw. Theory Tech.*, vol. 59, no. 8, pp. 1983–2000, Aug. 2011.

[17] E. Öjefors, F. Pourchon, P. Chevalier, and U. R. Pfeiffer, "A 160-GHz low-noise downconversion receiver front-end in a SiGe HBT technology," *Int. J. Microw. Wireless Technol.*, vol. 3, no. 3, pp. 347–353, Mar. 2011.

[18] E. Öjefors, B. Heinemann, and U. R. Pfeiffer, "A 220 GHz subharmonic receiver front-end in a SiGe HBT technology," in *IEEE RFIC Dig.*, Jun. 2011, Paper RMO-1C5.

[19] G. Avenier, M. Diop, P. Chevalier, S. Pruvost, J. Bouvier, G. Troillard, L. Depoyan, M. Buczko, N. Revil, S. Montusclat, A. Margain, S. T. Nicolson, K. H. K. Yau, D. Gloria, N. Loubet, N. Derrier, C. Leyris, S. Boret, D. Dutartre, S. P. Voinigescu, and A Chantre, "0.13 μm SiGe BiCMOS technology fully dedicated to mm-wave applications," *IEEE J. Solid-State Circuits*, vol. 44, no. 9, pp. 2312–2321, Sep. 2009.

[20] S. P. Voinigescu, E. Laskin, I. Sarkas, K. H. K. Yau, S. Shahramian, A. Hart, A. Tomkins, P. Chevalier, J. Hasch, P. Garcia, A. Chantre, and B. Sautreuil, "Silicon D-band wireless transceivers and applications," in *IEEE Asia–Pacific Microw. Conf. Dig.*, Dec. 2010, pp. 1857–1864.

[21] A. M. Mangan, S. P. Voinigescu, M. T. Yang, and M. Tazlauanu, "De-embedding transmission line measurements for accurate modelling of IC designs," *IEEE Trans. Electron. Devices*, vol. ED-53, no. 2, pp. 235–241, Feb. 2006.

[22] E. Laskin, P. Chevalier, A. Chantre, B. Sautreuil, and S. P. Voinigescu, "165-GHz transceiver in SiGe technology," *IEEE J. Solid-State Circuits*, vol. 43, no. 5, pp. 1087–1100, May 2008.

E. Dacquay (S'04) received the B.A.Sc. degree in computer engineering from the University of Waterloo, Waterloo, ON, Canada, in 2008, and is currently working toward the M.A.Sc. degree in electrical engineering at the University of Toronto.

His current research interests are in the areas of passive millimeter-wave imaging and detector modeling for silicon wafer scale imaging arrays.

A. Tomkins received the B.A.Sc. degree in engineering physics from Carleton University, Ottawa, ON, Canada, in 2006, and the M.A.Sc degree from the University of Toronto, Toronto, ON, Canada, in 2010.

He is currently with Peraso Technologies Inc., Toronto, ON, Canada, where he is a Millimeter-Wave Transceiver Designer.

K. H. K. Yau (S'03–M'11) received the B.A.Sc. degree (with distinction) in engineering physics from the University of British Columbia, Vancouver, BC, Canada, in 2003, and the M.A.Sc. and Ph.D. degrees in electrical engineering from the University of Toronto, Toronto, ON, Canada, in 2006 and 2011, respectively. His Ph.D. research concerned the area of on-wafer metrology techniques and compact modeling for nanoscale MOSFETs, advanced SiGe HBTs, and passive elements.

In 2011, he joined the Broadcom Corporation, Irvine, CA, where he is involved in the compact modeling of advanced nanoscale CMOS technologies.

Dr. Yau was the recipient of numerous scholarships, including an Undergraduate Research Award and a Post-Graduate Scholarship from the Natural Sciences and Engineering Council (NSERC) of Canada. He was also the recipient of an Achievement Award from the Association of Professional Engineers and Geoscientists of British Columbia.

E. Laskin received the B.A.Sc. (Hons) degree in computer engineering and M.A.Sc and Ph.D. degrees in electrical engineering from the University of Toronto, Toronto, ON, Canada, in 2004, 2006, and 2010, respectively.

In 2006, she was on a six-month internship with the IBM T. J. Watson Research Center, Yorktown Heights, NY. Her research interests include the design of high-speed and millimeter-wave integrated circuits with a focus on millimeter-wave imaging systems.

Ms. Laskin was a University of Toronto Scholar from 2000 to 2004. She was the recipient of the National Science and Engineering Research Counsel of Canada (NSERC) Undergraduate Student Research Award in industry and university in 2002 and 2003, the NSERC Postgraduate Scholarship, and the NSERC Canada Graduate Scholarship.

P. Chevalier (M'06) was born in Saumur, France, in 1971. He received the Engineering degree in science of materials from the University School of Engineers of Lille, Lille, France, in 1994, and the Ph.D. degree in electronics from the University of Lille, Lille, France, in 1998. His doctoral research concerned the development of 0.1-μm InP-based HEMT technologies.

In 1999, he joined Alcatel Microelectronics, Oudenaarde, Belgium, where he contributed to the start of RF BiCMOS and led the development of 0.35-μm SiGe BiCMOS technologies. In 2002, he joined STMicroelectronics, Crolles, France, to develop high-speed SiGe HBT's for 0.13-μm millimeter-wave BiCMOS. He is currently a Principal Engineer, Senior Member of Technical Staff, in charge of the process integration of advanced RF and millimeter-wave devices for CMOS derivatives technologies. He has authored or coauthored over 100 technical journal papers and conference publications.

Dr. Chevalier has been the chair of the Process Technology Subcommittee, IEEE Bipolar / BiCMOS Circuits and Technology Meeting. He belongs to the RF & AMS Technologies Working Group, ITRS, of which he leads the Silicon Bipolar and BiCMOS Subgroup.

A. Chantre (M'91–SM'97) was born in Reims, France, in 1953. He received the Engineering degree in physics from the Institut National des Sciences Appliquées de Lyon, France, in 1976, and the Ph.D. degree from the Université Scientifique et Médicale de Grenoble, Grenoble, France, in 1979. His doctoral research concerned deep-level optical spectroscopy (DLOS) in GaAs.

From 1979 to 1999, he was with the Centre National d'Etudes des Télécommunications (CNET), Grenoble, France. From 1985 to 1986, he was with AT&T Bell Laboratories, Murray Hill, NJ, where he was involved with deep-level defects investigations in silicon. From 1986 to 1992, he was in charge of a group that worked on the characterization of advanced silicon processes and devices. From 1993 to 1999, he worked within the GRESSI consortium between France Telecom CNET and CEA-LETI, as Head of a group involved in the development of advanced bipolar devices for submicrometer BiCMOS technologies. Since 2000, he has been with STMicroelectronics, Crolles, France, where he is currently manages the development of advanced SiGe BiCMOS devices and technology for RF, millimeter-wave, and optical communications applications. He has authored or coauthored over 150 technical papers related to his research. He holds 25 patents.

B. Sautreuil was born in La Rochelle, France, in 1954. He received the Engineer degree in material physics and Ph.D. degree in Ge solar cells for multicolor systems from INSA Lyon, Lyon, France, in 1979 and 1982, respectively.

In 1985, he joined Thomson Semiconductor (now STMicroelectronics), St. Egreve, France, in 1985, where he has been a Process, Maintenance, and Device Engineer. In 1991, he joined the Metallization Process Group, STMicroelectronics, Crolles, France, and then became involved with metal–implant area management, and the photo and etch area, including research and development. In 1999, join the Analog & RF Technology Research and Development Group, as an Assistant Manager of BiCMOS technology and passive component research and development. Since 2004, he has been involved with interface for BiCMOS RF and mixed signal technology platform customers. Since 2006, he has articipated in Si-photonics technologies evaluations.

S. P. Voinigescu (S'91–M'95–SM'02) received the M.Sc. degree in electronics from the Polytechnic Institute of Bucharest, Bucharest, Romania, in 1984, and the Ph.D. degree in electrical and computer engineering from the University of Toronto, Toronto, ON, Canada, in 1994.

From 1994 to 2002, he was first with Nortel Networks and later with Quake Technologies, Ottawa, ON, Canada, where he was responsible for projects in high-frequency characterization and statistical scalable compact model development for Si, SiGe, and III–V devices. He later conducted research on wireless and optical fiber building blocks and transceivers in these technologies. In 2002, he joined the University of Toronto, where he is currently a Full Professor. From 2008 to 2009, he spent a sabbatical year with Fujitsu Laboratories of America, Sunnyvale, CA. His research and teaching interests focus on nanoscale semiconductor devices and their application in integrated circuits at frequencies beyond 300 GHz.

Dr. Voinigescu is a member of the ITRS RF/AMS Committee and of the Technical Program Committees (TPCs) of the IEEE CSICS and BCTM. He was the recipient of Nortel's 1996 President Award for Innovation. He was a corecipient of the Best Paper Award of the 2001 IEEE CICC and the 2005 IEEE CSICS. He was also a recipient of the Beatrice Winner Award of the 2008 IEEE ISSCC. His students have been the recipients of Student Paper Awards presented at the 2004 VLSI Circuits Symposium, the 2006 SiRF Meeting, RFIC Symposium, BCTM, and the 2008 IEEE Microwave Theory and Techniques Society (IEEE MTT-S) International Microwave Symposium.